CAPTURE: Consistently Acquired Projections for Tuned and Robust Estimation
A Self-Navigated Respiratory Motion Correction Approach

Cihat Eldeniz, PhD,* Tyler Fraum, MD,† Amber Salter, PhD,‡ Yasheng Chen, DSc,§ H. Michael Gach, PhD,†‖ Parag J. Parikh, MD,‖ Kathryn J. Fowler, MD,† and Hongyu An, DSc*

Objectives: In this study, we present a fully automated and robust self-navigated approach to obtain 4-dimensional (4-D) motion-resolved images during free breathing.

Materials and Methods: The proposed method, Consistently Acquired Projections for Tuned and Robust Estimation (CAPTURE), is a variant of the stack-of-stars gradient-echo sequence. A 1-D navigator was consistently acquired at a fixed azimuthal angle for all stacks of spokes to reduce nonphysiological signal contamination due to system imperfections. The resulting projections were then "tuned" using complex phase rotation to adapt to scan-to-scan variations, followed by the detection of the respiratory curve. Four-dimensional motion-corrected and uncorrected images were then reconstructed via respiratory and temporal binning, respectively.

This Health Insurance Portability and Accountability Act–compliant study was performed with Institutional Review Board approval. A phantom experiment was performed using a custom-made deformable motion phantom with an adjustable frequency and amplitude. For in vivo experiments, 10 healthy participants and 12 liver tumor patients provided informed consent and were imaged with the CAPTURE sequence.

Two radiologists, blinded to which images were motion-corrected and which were not, independently reviewed the images and scored the image quality using a 5-point Likert scale.

Results: In the respiratory motion phantom experiment, CAPTURE reversed the effects of motion blurring and restored edge sharpness from 36% to 78% of that observed in the images from the static scan.

Despite large intra- and intersubject variability in respiration patterns, CAPTURE successfully detected the respiratory motion signal in all participants and significantly improved the image quality according to the subjective radiological assessments of 2 raters ($P < 0.05$ for both raters) with a 1 to 2-point improvement in the median Likert scores across the whole set of participants. Small lesions (<1 cm in size) which might otherwise be missed on uncorrected images because of motion blurring were more clearly depicted on the CAPTURE images.

Conclusions: CAPTURE provides a robust and fully automated solution for obtaining 4-D motion-resolved images in a free-breathing setting. With its unique tuning feature, CAPTURE can adapt to large intersubject and interscan variations. CAPTURE also enables better lesion delineation because of improved image sharpness, thereby increasing the visibility of small lesions.

Key Words: self-navigated, motion correction, complex phase rotation, gradient delay

I n the magnetic resonance imaging (MRI) of the body, respiratory motion has a negative impact on diagnosis, treatment planning, and therapeutic monitoring. Breath holding is often used in clinical practice.[1] However, breath holds typically last only tens of seconds, limiting spatial coverage and image quality. Breath holding can also be extremely difficult for some patients. In this respect, free-breathing MRI is highly desirable.

All free-breathing methods require a means of tracking respiratory motion. External devices such as respiratory bellows[2] and fiber optic sensors[3] can be used. However, the performance of respiratory bellows can be negatively impacted by the location of the bellows as well as by respiratory drift and large diaphragmatic excursion,[4] whereas fiber optic sensors are fragile and expensive.[5] The issues with external devices can be circumvented by MR acquisition-based strategies.

Navigator echoes are additional scans interleaved with the actual imaging scans and serve to track the position of the object being imaged.[6,7] Nevertheless, the additional radiofrequency excitation associated with the navigator echo degrades image quality as it disturbs the magnetization in the anatomic region of interest. Because of these limitations, inferring the respiratory state directly from the imaging data (ie, self-navigation) would be more preferable.

Various self-navigated retrospective rebinning schemes have been previously proposed. Image-based self-navigation using low-resolution images[8,9] requires manual delineation of a region of interest passing through the lung-liver interface, whereas automated methods are generally more desirable. Radial acquisitions offer the option of self-navigation because they frequently sample the center of k-space, where the acquired signal can show motion-related fluctuations.[10–13] One-dimensional (1-D) navigators extracted from the imaging k-space data have also been used for the self-navigated tracking of respiratory motion.[14–16] However, the k-space trajectories can be shifted away from their presumed locations because of gradient system imperfections, such as gradient delays and eddy currents.[17] These gradient imperfections can thus severely contaminate the self-navigation signal. Therefore, an acquisition scheme that is less prone to the adverse effects of these imperfections is highly desirable.

Because of intersubject variability as well as variations in physical scanning conditions, the usual ways of working with complex navigator data such as taking real parts or magnitudes do not result in a robust method that successfully detects respiratory motion in all cases.[18] A more generalized detection framework is needed.

In this study, we present a self-navigated, fully automated, free-breathing approach, termed as Consistently Acquired Projections for Tuned and Robust Estimation (CAPTURE). Our method is robust to

gradient imperfections and can adapt to intersubject and interscan variations. Deformable motion phantom experiments as well as in vivo experiments on healthy participants and liver tumor patients were performed to test if CAPTURE can detect respiratory motion reliably in all of these vastly different cases.

MATERIALS AND METHODS

A T_1-weighted stack-of-stars spoiled 3-D gradient-echo sequence with fat suppression has been previously proposed for motion correction.[11,19] Figure 1A illustrates this sequence. The partition (k_z) encoding is Cartesian, whereas the in-plane (k_x–k_y) acquisition is radial with a constant azimuthal increment of $\Delta\phi = 111.25°$; this increment provides an almost uniform in-plane coverage during any arbitrary scan duration.[20,21] This in-plane acquisition scheme has also been referred to as "golden-angle radial sampling" in the literature.[15,22] At each azimuthal angle, a stack of spokes is acquired by applying different levels of partition encoding.

Difficulty with the Original Stack-of-Stars Sequence: Spectral Contamination

As Figure 1A depicts, all stacks of spokes share a common point: the k-space center. In theory, this point is expected to show signal fluctuations exclusively due to respiratory motion, and hence can be used as a point navigator for deriving respiratory motion.[10,11,18] However, in practice, respiratory motion is not the only source of signal fluctuations at the k-space center, because gradient delays and eddy currents can significantly contaminate the spectrum of the point navigator.[23] Furthermore, this contamination is a function of the temporal order of the azimuthal angles in the acquisition.[24] Thus, golden-angle radial sampling contains numerous pseudo-periodicities, leading to physiologically irrelevant spectral peaks that can easily interfere with the respiratory spectral content.

Proposed Solution: Consistency in Navigator Direction and a Novel Detection Scheme

CAPTURE has 2 major components:

1. Consistently Acquired Projections (CAP-):
   As depicted in Figure 1B, CAPTURE is a variant of the stack-of-stars sequence, in which a navigator spoke along the k_x-axis replaces the first spoke in each stack. Based on the projection-slice theorem, the inverse Fourier Transform (FT) of this navigator yields a projection of all transverse magnetization onto the x-axis. In this study, the x-axis was chosen to be parallel to the superior-inferior (SI) axis, which is the axis of largest displacement for respiratory motion.[25] Because these navigators are always acquired at the same azimuthal angle, the gradient delays associated with them are expected to be the same.[26] To observe the spectral improvement achieved by this acquisition consistency, the spectrum of the CAPTURE-detected curve was compared with that of the point navigator signal,[11] which is contaminated by the angle-dependent variations described previously.

2. Tuned and Robust Estimation (-TURE):
   Magnetic field drift, background field inhomogeneity, and variations in receiver coil sensitivity profiles can lead to large intersubject and interscan variability in the navigator signal. As a result, developing a fully automated scheme that detects respiratory motion in all cases is challenging. It has been previously reported that the real parts, the imaginary parts, the magnitudes, and the phases of the projections, as well as the sum of the projection magnitudes, are not adequate to devise a detection scheme that works in all cases.[18] Our experience has confirmed this assertion. Figure 2 shows the detection results obtained by using various functions of the projections for one of the receiver coils. Possibly because of the aforementioned factors that change from scan to scan, none of these functions yielded a reasonable respiration curve. To overcome this difficulty, we devised the following
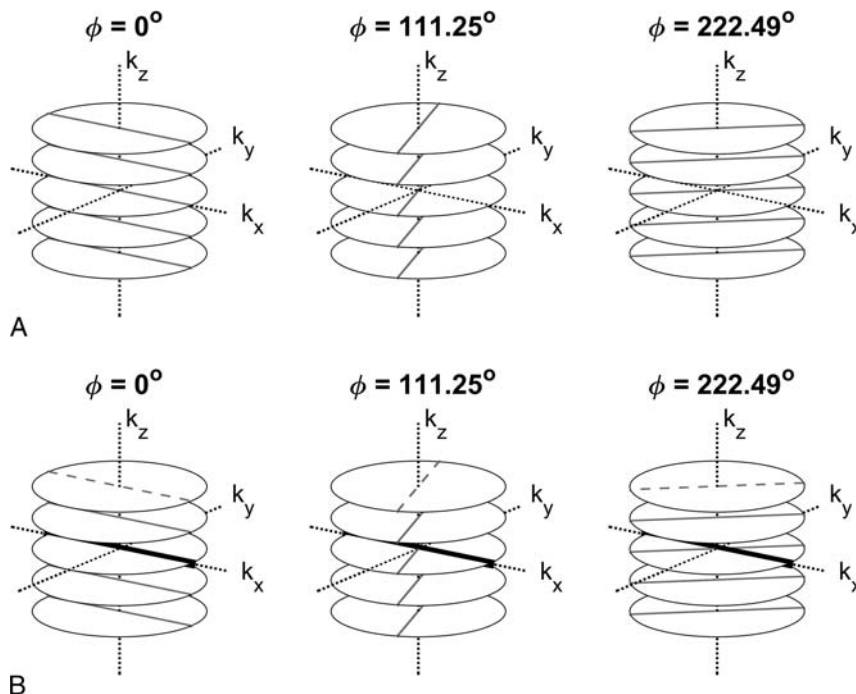

FIGURE 1. Acquisition scheme for a conventional 3-D golden-angle stack-of-stars sequence (A) and CAPTURE (B). In CAPTURE, the dashed spokes were replaced with the navigators shown by thick black lines. In this example, the navigators are always acquired at the same azimuthal angle (0°) such that they experience similar gradient delays and eddy currents.
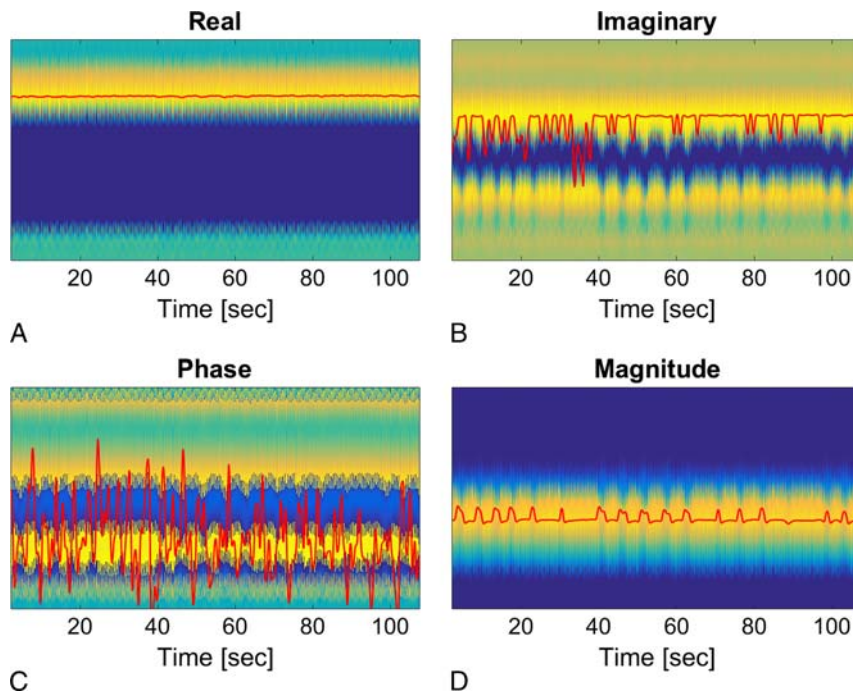
FIGURE 2. Maximum detection using (A) real and (B) imaginary parts, as well as (C) phase and (D) magnitude, of the complex projections. The red curves were obtained by filtering the maximum detection results with a low-pass filter with a 1 Hz cutoff frequency. None of these schemes could capture the underlying respiratory content.

detection scheme that can adapt to intersubject and interscan variability by "tuning" the phase of the projections. Figure 3 illustrates the process of signal "tuning," which is detailed as follows:

- The first 10 stacks of spokes were discarded to ensure steady-state conditions.
- To reduce noise, the navigator k-space data were apodized using a Hamming window. After a 1-D inverse FT, the resulting complex projections from all stacks of spokes received through coil i were placed as columns of a 2-D matrix, $\mathbf{P}_i = \mathbf{P}_i[x,n]$, where x is the index for the physical locations on the SI axis and n is the stack-of-spokes index or, equivalently, the discrete time index.
- A "tuning" process was then performed by phase-rotating $\mathbf{P}_i$'s over the full phase range, $(0,360°]$, via 100 different complex scalar multiplications $e^{-j\alpha_m}\mathbf{P}_i$, where $\alpha_m = m \times 3.6°$ with $m = 1, 2,…, 100$. Four representative phase rotations are demonstrated in Figure 3. For each α_m, a respiratory curve $r_{i,m}[n]$ was obtained by detecting the location of the peak along each column of $A_{i,m} \triangleq \mathrm{Re}\{e^{-j\alpha_m}\mathbf{P}_i\}$, where $\mathrm{Re}\{.\}$ is the real part operator. The 4 illustrations of $A_{i,m}$ and $r_{i,m}[n]$ corresponding to the 4 phase rotation angles $\alpha_m = 61.2°$, $165.6°$, $259.2°$, and $327.6°$ for coil 3 are shown in Figure 3A.
- The detected respiratory curves, $r_{i,m}[n]$, were Fourier transformed, yielding $R_{i,m}(f)$. Examples of $R_{i,m}(f)$ are shown in Figure 3B.
- A temporospectral quality metric was then defined:

$$Q_{i,m} = \frac{\int_{0.1\,\mathrm{Hz}}^{0.5\,\mathrm{Hz}} \left|R_{i,m}(f)\right| df}{\int_{0.8\,\mathrm{Hz}}^{\infty} \left|R_{i,m}(f)\right| df} \times \left(\frac{1}{\max\limits_{n} r_{i,m}[n] - \min\limits_{n} r_{i,m}[n]} \right) \quad (1)$$

The first term in the product favors respiratory content over system-related spectral contamination, whereas the second term penalizes the peak-to-trough range of the detected curve. Figure 4 illustrates the

importance of this second term, that is, the range term. The motivation is as follows: For a number of tuning angles, parts of the respiratory curve can appear on spatially separated bands. The abrupt signal changes observed in these cases can lead to spectral leakage into the respiratory range of frequencies, misleading the detection procedure. The second term penalizes these problematic abrupt changes, promoting only truly respiratory curves.

Figure 3C shows $Q_{i,m}$ values as a function of phase rotations.

- Finally, the best coil and phase rotation were chosen according to the following:

$$(i^*, m^*) = \underset{(i,m)}{\arg\max} \; Q_{i,m} \quad (2)$$

A low-pass filter with a cut-off frequency of 1 Hz was used for removing physiologically irrelevant contamination. To avoid filtering-related distortion, Savitzky-Golay filtering output was used for replacing the samples at the two ends. The resulting respiratory curve was used for sorting the data into 10 respiratory bins, each with an equal number of spokes.

Importance of Phase Tuning

To demonstrate the importance of phase tuning, respiratory curve detection was performed by using the real part of the complex projections without any tuning, and the result was compared with the tuned detection of CAPTURE.

Experiments

All experiments were performed on a simultaneous PET/MRI scanner with 3 T field strength (Siemens Biograph mMR [VB20P]; Siemens Healthcare, Erlangen, Germany).
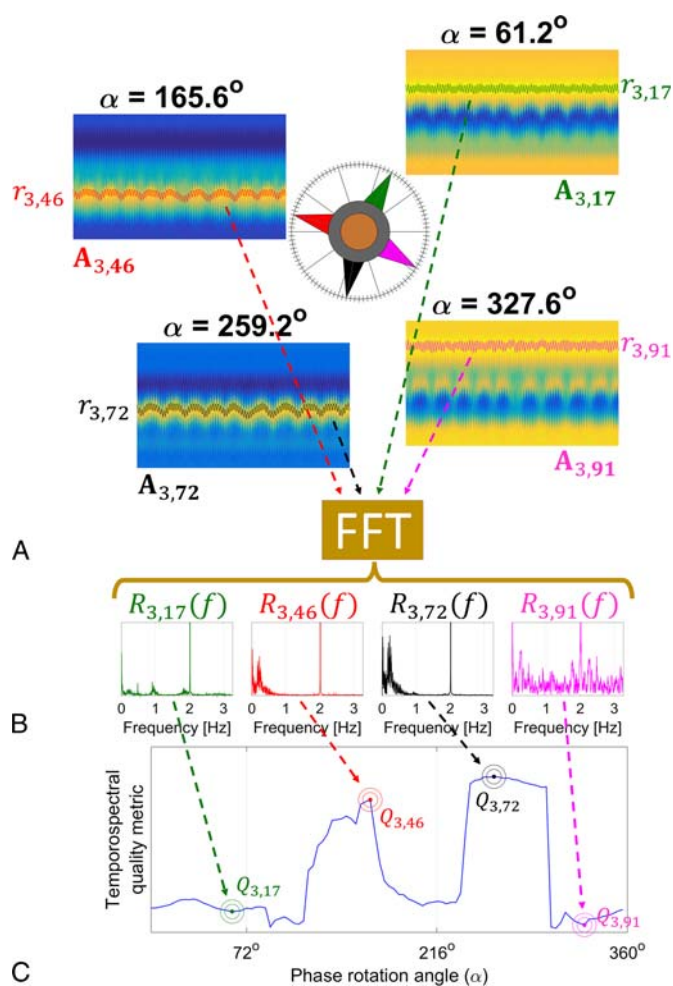
FIGURE 3. Complex signal tuning scheme. Four representative phase rotations for a chosen coil (coil 3) are depicted. In panel A, the *x*-axis, the *y*-axis, and the color axis represent time, navigator axis, and the signal intensity of $A_{i,m}$, respectively. The derived unfiltered respiratory curves $r_{i,m}[n]$ (overlaid curves in panel A) are also provided. The frequency spectra and their corresponding temporospectral quality metric values for the 4 representative phase rotations are shown in panels B and C, respectively. In this example, the optimal phase rotation angle, which provided the highest temporospectral quality metric value, was found to be 259.2°.

Phantom Experiments

A respiratory motion phantom (Chest-R) was built using a Harvard Apparatus Large Animal Respiration Pump (Model 607) with an adjustable frequency and amplitude. Chest-R contained a balloon immersed in sodium polyacrylate gel. The balloon was inflated and deflated by the pump. Three different motion frequencies (corresponding to 10, 20, and 30 rpm) and 2 air volumes (400 and 600 cc) were tested. Static imaging was also performed to obtain the ideal image sharpness at the air-gel interface.

The CAPTURE acquisition parameters were as follows: TE/TR = 1.99 ms/3.84 ms, matrix size = 320 × 320, field of view = 240 mm × 240 mm, slab thickness = 163.2 mm, number of partitions = 48, partial Fourier factor = 6/8, reconstructed slices per slab = 96 (yielding a slice thickness of 1.7 mm). The resulting voxel size for the phantom study was $0.75 \times 0.75 \times 1.7 \text{ mm}^3$.

Human Experiments

This Health Insurance Portability and Accountability Act–compliant study was performed after the approval of our institutional review board. Both healthy volunteers and liver tumor patients were recruited between November 1, 2016, and May 24, 2017, and all participants provided written informed consent. No data were excluded in our analysis.

All participants were imaged in the head-first supine position. A flex body coil with 2 elements (BO1-2) was placed anteriorly over each participant, and a spine coil with multiple elements (SP1-8) was positioned posteriorly in the patient table. A total of 3 or 4 spine coil elements were automatically selected by the MR scanner to achieve sufficient coverage of the user-specified imaging volume.

Healthy Volunteer Experiments

Ten healthy volunteers (median age [interquartile range] in years: 29 [24-33], all men) were scanned in coronal, sagittal, and transversal orientations.

The CAPTURE acquisition parameters were as follows: TE/TR = 1.69 ms/3.54 ms, matrix size = 320 × 320, field of view = 360 mm × 360 mm, slab thickness = 288 mm, number of partitions = 48, partial Fourier factor = 6/8 (giving a temporal resolution of 153.52 ms for the navigator), reconstructed slices per slab = 96 (yielding a slice thickness of 3 mm). The resulting voxel size was $1.125 \times 1.125 \times 3 \text{ mm}^3$. The number of azimuthal angles was 2000, resulting in a total acquisition time of 5 minutes and 7 seconds.

Moreover, to explain why phase tuning works, we performed 2 scans using single-slice gradient recalled echo (GRE) sequences on 1 healthy volunteer. The acquisitions were sagittal with the readout axis lying along the SI axis of the subject. The first GRE protocol was as follows: TE/TR = 3.1 ms/5.6 ms, slice thickness = 3 mm, matrix size = 192 × 126, in-plane resolution = 1.56 × 1.56 mm, number of sequence repetitions = 500, total scan time = 67 seconds. Generalized autocalibrating partially parallel acquisitions[27] was used for accelerating the acquisition (acceleration factor $R = 2$) so that each image could be acquired in 134.4 ms, making it possible to observe the liver's motion during respiration. The second GRE protocol was the same as the first one except that the slice thickness was set to 250 mm. This thick excitation yielded the projection of the signals in a large spatial region onto the sagittal plane. The thick-slice acquisition was therefore useful for mimicking the projections used by CAPTURE, whereas the thin-slice acquisition provided a better visualization of the liver's anatomical location along the SI axis. Both sets of GRE scans were reconstructed into complex images for each receiver channel, and phase tuning was applied to observe the variations in the signal intensities. The SI projections that would mimic the projections of CAPTURE were obtained by taking the inverse FT of the central *k*-space lines of the thick-slice GRE data after apodization. Only the data from the middle spine coil element are going to be shown for brevity.

Liver Tumor Patient Experiments

Twelve patients (median age [interquartile range] in years: 59.5 [56-66.5], 4 women) with various liver tumors were recruited. Six patients had primary hepatic malignancies, whereas the other 6 had metastatic disease from an extrahepatic primary (Table 2).

All images for the liver tumor patients were acquired in the sagittal plane with the same parameters used for the healthy volunteers, except for an increase in the number of slices (for greater spatial coverage) in several patients and a higher in-plane resolution (0.8 mm rather than 1.125 mm) in 1 patient. Depending on the acquisition parameters, the temporal resolution of the navigator ranged from 153.52 to 189.10 ms. The scan of 1 patient was terminated earlier than planned because of miscommunication, and hence only 82% of the data were acquired. Nevertheless, this partial dataset
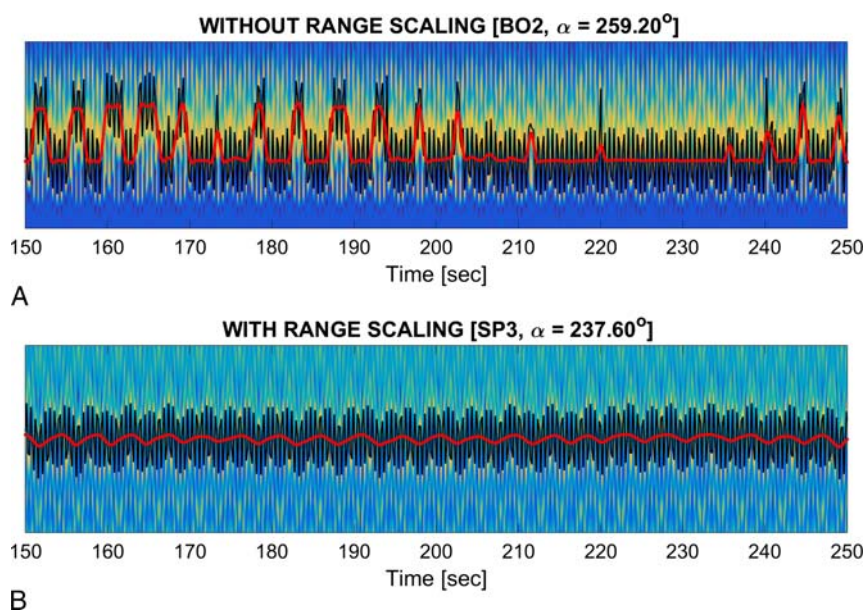
FIGURE 4. Importance of range scaling. If the range of the signal is not penalized (A), the detection algorithm may select a curve with nonphysiological abrupt changes that can introduce a large amount of spectral leakage into the respiratory band. However, if the range is penalized (B), this spectral leakage is prevented, and the algorithm will instead favor curves reflecting the true respiratory content.

was still included in our analysis because the image quality was not substantially affected by the missing spokes.

Because some patients may change their breathing patterns significantly during an MRI session, we also examined if CAPTURE can successfully detect respiratory motion in such cases. For this purpose, one of the 10 healthy volunteers was asked, in a separate experiment, to intentionally change his breathing pattern (so as to include deep breathing and breath holding) during image acquisition. However, only the images from his normal breathing experiment were included in the radiological review.

Reconstruction

The imaging data were first inverse Fourier transformed along the partition encoding direction to enable slice-by-slice processing. A reconstruction approach with a motion smoothness constraint similar to that of the XD-GRASP approach[15] and a spatial smoothness constraint[28,29] was then applied to each slice to reconstruct 10 respiratory phase images. By binning the same k-space data into 10 consecutive temporal (rather than physiological) bins, motion-uncorrected images having the same signal-to-noise ratio as the CAPTURE-reconstructed images were also obtained for a direct comparison.

Performance Evaluation in Phantom

Line profiles across the air-gel interface were used to assess performance. Apparent slopes, which served as a metric for motion correction adequacy, were measured by using a line across the air-gel interface.

Performance Evaluation In Vivo

Motion-corrected and uncorrected images were placed side by side in a pairwise fashion with left-right randomization for each participant. Two radiologists, who were blinded to the corrected versus uncorrected datasets, reviewed the images independently using a Likert scale of 1 to 5 (1, very blurry; 2, blurry; 3, intermediate; 4, sharp; 5, very sharp). The radiologists assessed the largest liver

finding (for liver tumor patients only), the largest portal vein (for both healthy volunteers and liver tumor patients), and the lung-liver interface (for both healthy volunteers and liver tumor patients). For each rater, changes in image quality were statistically assessed by using the signed rank test.

RESULTS

Improvement in Spectral Quality

Figure 5 compares the spectra obtained by the k-space center point navigator versus CAPTURE for 2 different participants. The point navigator spectra are severely contaminated because of system imperfections such as gradient delays and eddy currents. This contamination generated numerous artificial signal peaks at frequencies ranging from 0.5 to 3 Hz (Fig. 5, A and C). Because the signal contamination located near 0.5 Hz is within or close to the physiological respiratory frequency range, it is extremely challenging to remove this contamination without distorting the true respiratory signal. If the participant has a low primary respiratory frequency (eg, healthy volunteer 3), the signal contamination may be removed using a low-pass filter with a cutoff frequency between the primary respiratory frequency and 0.5 Hz (Fig. 5A). However, if the primary respiratory frequency is high (eg, healthy volunteer 1), the separation of respiratory content and signal contamination using conventional filtering techniques becomes impossible (Fig. 5C). In contrast, contamination in the CAPTURE spectra is significantly reduced and mainly concentrated around 2 Hz (Fig. 5, B and D). This nonphysiological peak is well separated from the respiratory content and can be easily removed by low-pass filtering.

Importance of Phase Tuning

Figure 6 depicts the significance of phase tuning for one of the healthy volunteers. As shown in Figure 6, A and B, the real part–based detection (before complex phase rotation) led to an almost flat curve with little respiratory content. In contrast, the optimal phase rotation resulting from CAPTURE tuning significantly enhanced the respiratory content buried in the data (Fig. 6, C and D).
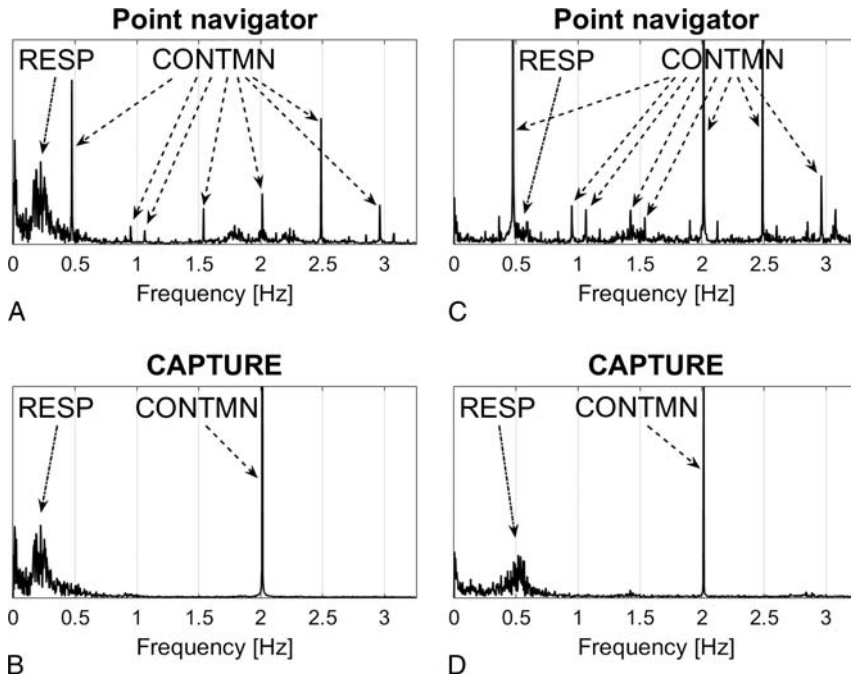
FIGURE 5. Comparison of spectra of signals obtained by the point navigator and CAPTURE from 2 representative participants. Panels A and B are from healthy volunteer 3, whereas panels C and D are from healthy volunteer 1. The nonphysiological contamination (CONTMN) introduced by the 2 methods was indicated by dashed arrows, whereas the true respiratory content (RESP) was indicated by dash-dot arrows. The contamination in the case of the point navigator is clearly more widespread and leads to severe interference with the respiratory content, especially for healthy volunteer 1.
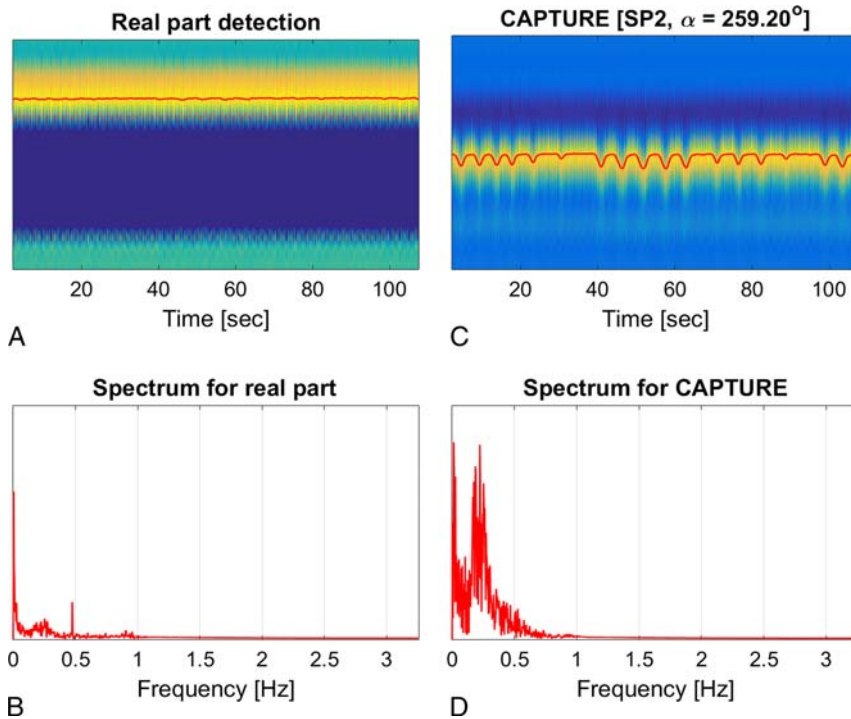
FIGURE 6. Importance of tuning complex projections before respiratory curve detection. (A) The result (red curve) obtained by maximum detection on the real part of the raw complex projections. (B) The corresponding spectrum. (C) The result (red curve) obtained by maximum detection on the real part of the phase-tuned complex projections. (D) The corresponding spectrum. Whereas the spectrum of the real part–based detection shown in panel B exhibits weak respiratory content, CAPTURE tuning clearly amplifies the respiration-related spectral content as shown in panel D.
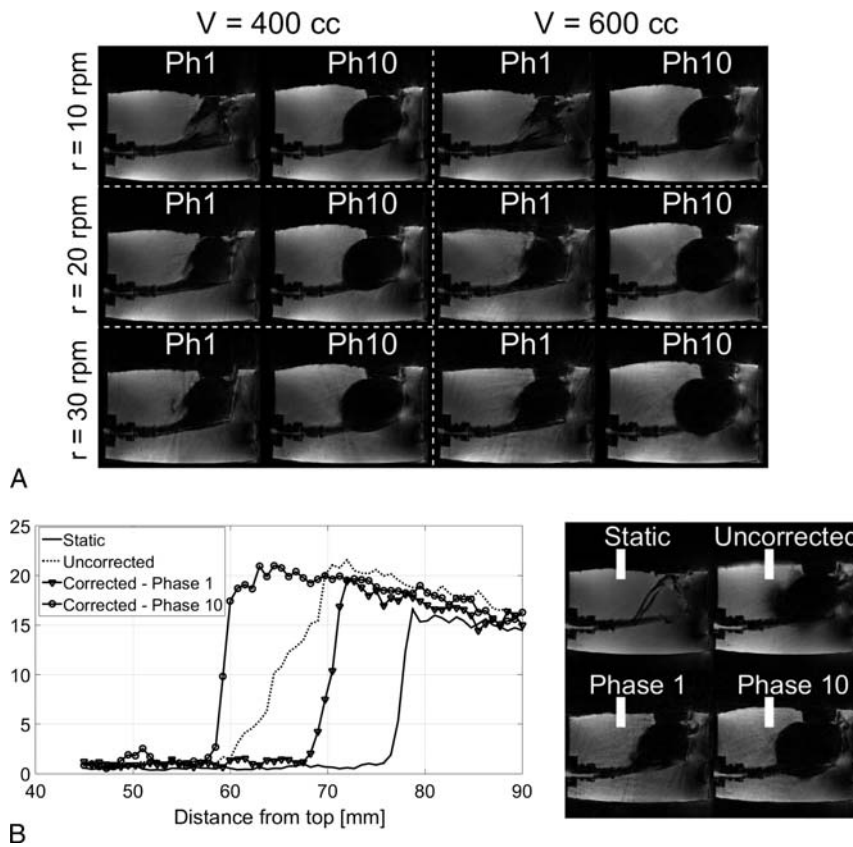
FIGURE 7. (A) The first and last respiratory phases for the respiration phantom under 6 different motion settings. (B) Averaged intensity profiles from the same location of the air-gel interface for the largest-volume highest-speed setting (V = 600 cc, r = 30 rpm). The averaging was performed across 15 adjacent profiles indicated by the white bands in the right-hand-side images. The slopes for the static experiment, the uncorrected image, and phases 1 and 10 of the motion-corrected dataset were found to be 5.17, 1.86, 4.06, and 3.99 (arbitrary unit), respectively.

FIGURE 8. The uncorrected images and 3 representative respiratory phases from the CAPTURE-corrected dataset of one of the healthy volunteers.

Phantom Experiments

CAPTURE successfully resolved respiratory motion under all six different settings (Fig. 7A). Figure 7B shows the line profile plots across the air-gel int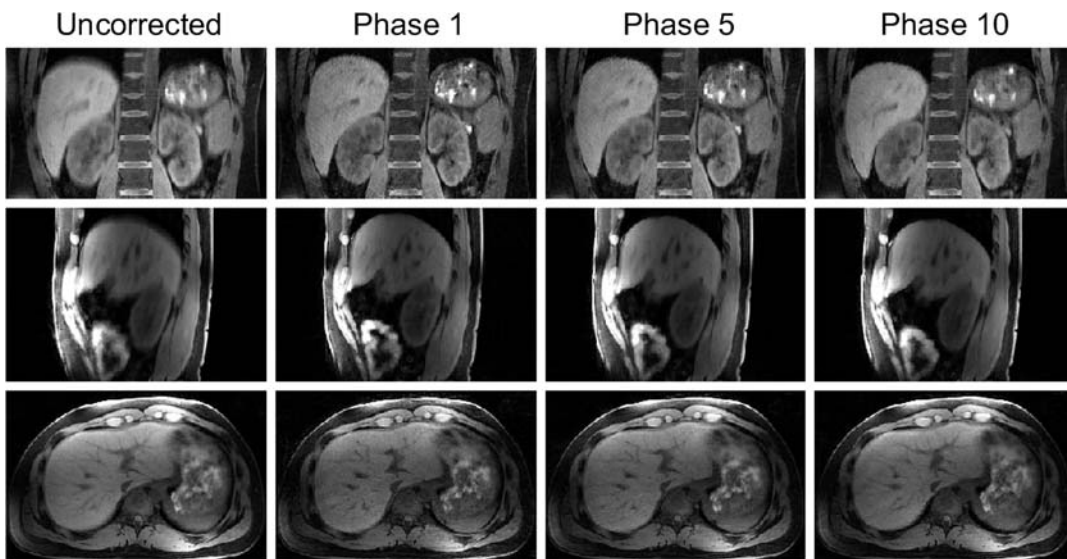erface in static, motion-uncorrected, and motion-corrected images. The slope across the air-gel interface, which was diminished to 36% of the static case in the motion-uncorrected image, was recovered to 78% of the static case in the motion-corrected images.

Human Experiments

CAPTURE improved image sharpness in all 3 imaging orientations (Fig. 8), implying that CAPTURE is able to resolve respiratory motion regardless of the imaging orientation.

Figure 9 illustrates the effects of phase tuning on the thick-slice GRE data for 2 phase rotation angles. The red curves in the left column are the detected respiratory curves obtained by applying peak detection on phase-rotated projections. The images in the middle column depict the phase-rotated real parts for a sequence repetition of the thick-slice GRE acquisition, with the overlaid black curve being the projection computed from the same repetition and the red asterisk marking the peak of the projection. The images in the right column are from a

sequence repetition of the thin-slice GRE acquisition and provide a better anatomical reference. This figure shows that the phase-tuned real part operator selectively highlights different parts of the body for different phase rotation angles. If a suitable phase rotation is applied, this operation can highlight an anatomical region that moves significantly with respiration. Figure 9A illustrates an example for this phenomenon where the highlighted region forms a bright band on the liver area. In contrast, for some phase rotation angles, phase tuning highlights structures that do not move with respiration, in which case the detected curve will not represent respiration (Fig. 9B). A quality metric similar to the one used in CAPTURE can be used here as well for selecting the angle providing the curve with the best respiratory characteristics. This figure also explains why the ordinary real part and imaginary part operators fail to work in some cases—because of large intersubject and interscan phase variability, these operators might be highlighting anatomical regions that do not move much with respiration.

Supplemental Digital Content 1 (Video, http://links.lww.com/RLI/A365) demonstrates how the phase-tuned real part operator highlights different anatomical structures as the tuning angle sweeps through
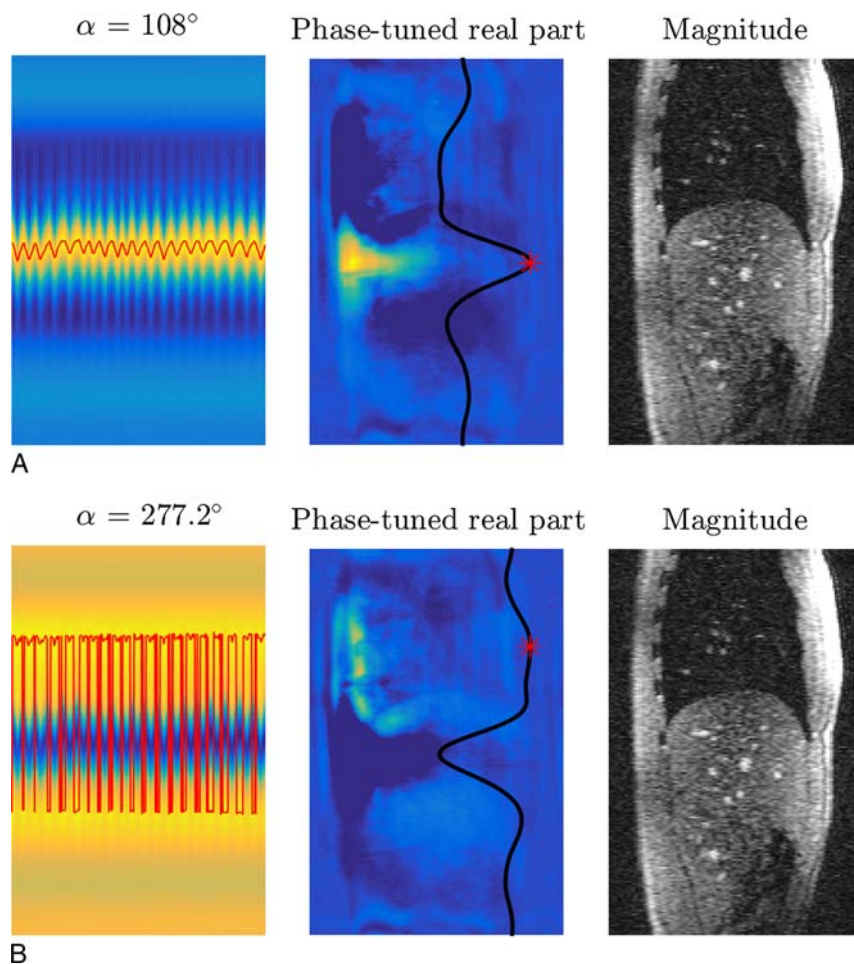
FIGURE 9. The importance of CAPTURE's phase tuning and how it helps respiratory motion detection are illustrated on the same data by using a suitable (A) and a poor (B) phase tuning angle. The images in the left column exhibit the phase-tuned real parts of the projections. The overlaid red curves are the detected respiratory motion curves obtained by peak detection. The images in the middle column are the phase-tuned real part images from a single sequence repetition of the thick-slice GRE acquisition. The overlaid black curves are the corresponding projections for that particular sequence repetition with the red asterisk indicating the peak of the projection. The images in the right column are thin-slice GRE images that provide a better anatomical reference.

TABLE 1. Age, Sex, CAPTURE-Detected Dominant Respiratory Frequency (ie, the Location of the Peak Within [0.1,0.5] Hz in the Spectrum of the Detected Curve), and Measured End-Inspiration to End-Exhalation Motion Range of Liver Dome in Motion-Resolved Images of CAPTURE for Healthy Volunteers

	Age, y	Sex	Respiration Frequency, Hz	Motion Range, mm
Healthy volunteer 1	22	M	0.52	16.9
Healthy volunteer 2	46	M	0.35	18.0
Healthy volunteer 3	31	M	0.22	20.2
Healthy volunteer 4	32	M	0.16	27.0
Healthy volunteer 5	24	M	0.36	18.0
Healthy volunteer 6	30	M	0.15	23.6
Healthy volunteer 7	28	M	0.37	16.9
Healthy volunteer 8	28	M	0.24	15.8
Healthy volunteer 9	62	M	0.24	16.9
Healthy volunteer 10	23	M	0.37	23.6

The median respiratory frequency was 0.30 Hz (interquartile range, 0.22–0.37 Hz).
M indicates male.

(0°,360°]. On the other hand, Supplemental Digital Content 2 (Video, http://links.lww.com/RLI/A366) demonstrates how the abdominal region highlighted by the phase rotation of 54° in the thick-slice GRE image moves with respiration. The corresponding magnitude image was also provided for the visualization of anatomical structures.

Large variations were observed in primary respiratory frequencies and liver dome motion ranges (Tables 1 and 2). Moreover, the respiratory patterns varied greatly not only across participants, but also for a given participant within the same imaging session (Fig. 10). Despite this high variability, CAPTURE was able to extract the respiratory content from all datasets in a fully automated manner by adapting to the unique characteristics of the participant's respiratory pattern. This adaptability is demonstrated by the wide range of optimal rotation angles and coil elements listed in Tables 3 and 4. It is worth noting that the automated tuning process usually favored a coil element that provided a good spatial coverage of the lung-liver interface. The robustness of CAPTURE is also demonstrated by the results of our experiment

involving a participant instructed to intentionally alter his breathing pattern (Fig. 11).

In the study of liver tumor patients, the lesions became more conspicuous in CAPTURE-corrected images (Fig. 12). Some small lesions (<1 cm in size) that may have been missed on the uncorrected images because of motion blurring were depicted clearly in the CAPTURE images.

For the healthy volunteers, rater 1 scored CAPTURE images higher for all coronal and sagittal image sets, and for 7 of 10 transverse image sets (for the remaining 3 cases, corrected and uncorrected images were scored equally). Rater 2 reported improvement in all cases in all 3 orientations. For the liver tumor patients, rater 1 scored CAPTURE images higher in 11 of 12 cases (for the remaining case, the corrected and uncorrected images were scored equally). Rater 2 reported improvement in all cases. It is worth noting that the Likert scores of the 4 cases rated equally were 4, 4, 5, and 5, which are already close to or equal to the maximum Likert score that can be given. When assessed

TABLE 2. Age, Sex, CAPTURE-Detected Dominant Respiratory Frequency (ie, the Location of the Peak Within [0.1,0.5] Hz in the Spectrum of the Detected Curve), and Measured End-Inspiration to End-Exhalation Motion Range of Liver Dome in Motion-Resolved Images of CAPTURE for Liver Tumor Patients

	Age, y	Sex	Diagnosis	Respiration Frequency, Hz	Motion Range, mm
Patient 1	56	M	Metastatic disease (colorectal cancer)	0.35	23.6
Patient 2	61	M	Hepatocellular carcinoma	0.21	19.1
Patient 3	66	M	Hepatocellular carcinoma	0.26	12.4
Patient 4	35	F	Metastatic disease (colorectal cancer)	0.19	10.1
Patient 5	67	F	Metastatic disease (colorectal cancer)	0.34	10.4
Patient 6	57	M	Hepatocellular carcinoma	0.27	11.2
Patient 7	74	M	Hepatocellular carcinoma	0.14	34.9
Patient 8	72	M	Hepatocellular carcinoma	0.26	12.4
Patient 9	58	M	Hepatocellular carcinoma	0.46	24.8
Patient 10	56	F	Metastatic disease (breast cancer)	0.26	10.1
Patient 11	55	F	Metastatic disease (neuroendocrine carcinoma)	0.22	16.9
Patient 12	61	M	Metastatic disease (ocular melanoma)	0.24	14.6

The median respiratory frequency was 0.26 Hz (interquartile range, 0.22-0.30 Hz).
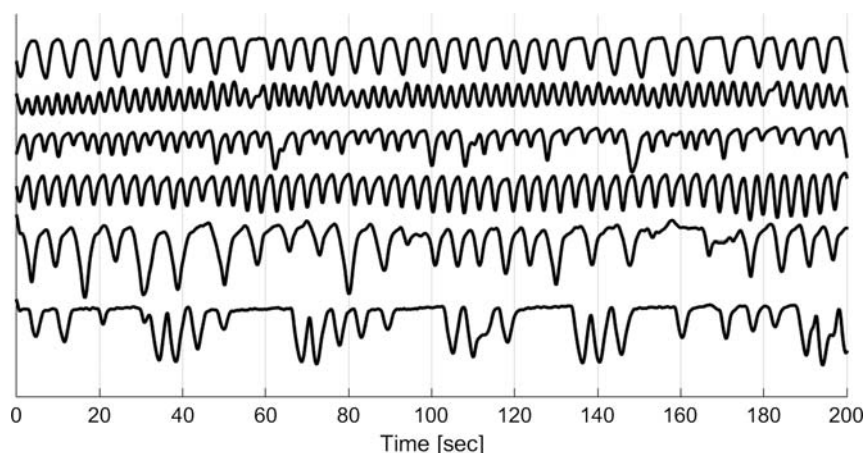M indicates male; F, female.

FIGURE 10. From top to bottom: detected respiratory curves from 3 healthy volunteers and 3 liver tumor patients. The breathing patterns vary greatly not only across subjects, but also for a given participant within the same imaging session.

statistically, CAPTURE had significantly higher image quality scores for both readers in both the healthy volunteers and the liver tumor patients (Fig. 13). The improvement in the median Likert scores ranged from 1 to 2 points across the whole set of participants.

DISCUSSION

CAPTURE has 2 unique features: (1) the consistent acquisition of projections (CAP-) that substantially alleviates the effects of gradient system imperfections and hence provides "cleaner" signals, removing the need for heavy filtering or complicated pattern recognition methods; and (2) the tuned and robust estimation (-TURE) process that adjusts the phase of the complex projections to allow for a fully automated respiratory signal detection, even in the presence of large intersubject and interscan variations.

In this study, CAPTURE was able to resolve respiratory motion both in a phantom and in human participants, the latter of which can exhibit a wide variety of respiration patterns. Moreover, in liver tumor patients, some focal lesions were more clearly depicted by CAPTURE images.

Azimuthal angle-dependent spectral contamination is significantly reduced for CAPTURE because the projections are always acquired at the same azimuthal angle across all stacks of spokes. In addition, CAPTURE uses the position of the peak along each of the 1-D projections, rather than the signal intensity itself. Therefore, the factors that can cause signal contamination become less problematic. Furthermore, CAPTURE makes no assumptions about the MRI signal except that respiration frequencies are below 1 Hz. Therefore, baseline correction, detrending, principal component analysis, or other preprocessing steps that may distort the true physiological response are not necessary. In contrast, the point navigator approach introduced by Grimm et al[11] uses the signal intensity variations at the center of the k-space to track respiratory motion. Many factors including gradient delays, eddy currents, and off-resonance effects can therefore confound respiratory tracking in this approach.[30] As a result, angle-based signal detrending and heavy filtering have to be applied to remove azimuthal angle-dependent contamination, but these processes may distort the actual physiological signal. On the other hand, the XD-GRASP method[15] uses the $k_x = k_y = 0$ points along the k_z-axis to form a 1-D navigator. A principal component analysis is then performed on the corresponding projections. The principle component with the highest spectral peak within the 0.1 to 0.5 Hz range is finally chosen for deriving respiratory motion. We have found that this principle component can still have a

TABLE 3. Optimal Coils and Phase Rotation Angles Given by CAPTURE for Healthy Participants

	Sagittal		Coronal		Transversal	
	Coil	**Angle**	**Coil**	**Angle**	**Coil**	**Angle**
Healthy volunteer 1	SP2	144.0°	SP2	126.0°	SP2	122.4°
Healthy volunteer 2	SP2	162.0°	SP2	183.6°	SP2	324.0°
Healthy volunteer 3	SP2	259.2°	SP2	223.2°	BO1	18.0°
Healthy volunteer 4	SP2	144.0°	BO2	147.6°	SP2	259.2°
Healthy volunteer 5	SP2	136.8°	SP4	79.2°	SP2	169.2°
Healthy volunteer 6	SP1	349.2°	BO2	306.0°	SP2	306.0°
Healthy volunteer 7	SP2	144.0°	SP2	306.0°	SP2	205.2°
Healthy volunteer 8	SP2	324.0°	SP2	93.6°	SP2	327.6°
Healthy volunteer 9	SP1	126.0°	SP2	180.0°	SP1	100.8°
Healthy volunteer 10	BO1	172.8°	BO2	82.8°	SP3	54.0°

BO[i] indicates elements of the flex body coil placed on the chest of the participant; SP[i], elements of the spine coil placed in the scanner table that are next to the spine of the participant.

TABLE 4. Optimal Coils and Phase Rotation Angles Given by CAPTURE for Patient Participants

	Sagittal	
	Coil	**Angle**
Patient 1	SP2	334.8°
Patient 2	SP3	237.6°
Patient 3	SP3	241.2°
Patient 4	SP4	356.4°
Patient 5	BO2	190.8°
Patient 6	SP2	72.0°
Patient 7	SP3	280.8°
Patient 8	SP3	32.4°
Patient 9	SP3	338.4°
Patient 10	SP1	133.2°
Patient 11	BO2	180.0°
Patient 12	SP5	39.6°

BO[i] indicates elements of the flex body coil placed on the chest of the participant; SP[i], elements of the spine coil placed in the scanner table that are next to the spine of the participant.

high amount of nonphysiological signal contamination because of the same confounding factors mentioned previously for the point navigator method.

The navigators of CAPTURE can be flexibly placed along the direction most sensitive to motion regardless of the imaging orientation. Nonetheless, the direction of the 1-D navigators of XD-GRASP is fixed by the imaging orientation, which may reduce sensitivity for motion detection if the navigator direction (ie, the z direction) does not coincide with the axis of the largest displacement, that is, the SI axis.

In this study, the navigator resolution of CAPTURE was 1.125 mm because the navigators were acquired using the readout gradient. The spatial resolution of the XD-GRASP navigators, however, is limited by the slice thickness of the experiment, which was 3 mm both in this study and in the XD-GRASP study. Hence, CAPTURE may enable higher navigator spatial resolution than XD-GRASP, increasing the accuracy of detection.

CAPTURE tunes the signal through complex phase rotation and finds the optimal phase rotation angle that works best for the data at hand. The respiratory curve detection in CAPTURE is fully automated and takes less than 4 seconds on a 64-bit Windows 7 PC with 32 GB of memory and an Intel Xeon CPU (3.50 GHz). The signal tuning process makes it possible to adapt to large intersubject variations. Ordinary real part– and imaginary part–based detection schemes are already included in CAPTURE because they correspond to 2 of the 100 phase rotations that are applied (real part detection visited for $\alpha_{100} = 360°$, imaginary part detection visited for $\alpha_{25} = 90°$). It is also worth noting that, although CAPTURE uses the phase rotation yielding the highest quality metric, usually a number of neighboring phase rotations yield similar quality metric values, and these angles can also provide reasonable respiration curves. Supplemental Digital Content 1 (Video, http://links.lww.com/RLI/A365) demonstrates that as the tuning angle changes, the highlighting in the image changes smoothly. This smoothness translates into plateaus in temporospectral quality metric plots, implying that not a single angle but a multitude of them should work well for binning purposes, as long as the bright band falls onto a region that moves significantly with respiration.

It can be argued that phase tuning might highlight static structures or regions with irrelevant motion, which might distort the detected respiratory curve. It is true that a large range of tissues can be highlighted as the tuning operation sweeps through the entire set of angles within (0°,360°]. However, the temporospectral quality metric has a stringent criterion for automatically selecting the tuning angle that yields the curve most representative of the underlying respiration.

More than 1 navigator along different directions can also be used for detecting 2 or more different types of motion. For instance, 1 navigator can be used for respiratory motion, whereas another can be used for cardiac motion. It is also possible to acquire multiple instances of the same navigator within the same stack of spokes to achieve a higher sampling rate. The navigation scheme of CAPTURE can also be easily adapted to other Cartesian and non-Cartesian sequences.

CAPTURE has a number of limitations. For instance, 1 imaging partition is replaced by a 1-D navigator, leading to a 2% to 3% loss in imaging efficiency, whereas both the point navigator scheme[11] and the XD-GRASP scheme[15] estimate respiratory motion based solely on the imaging data without a loss in imaging efficiency. In addition, neither these 2 methods nor CAPTURE corrects for gradient delays. A gradient delay correction scheme similar to that proposed by Moussavi
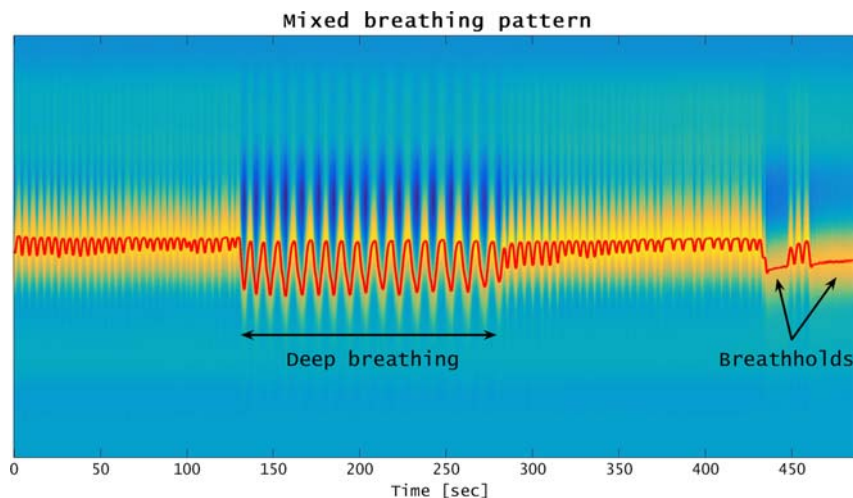
FIGURE 11. Detected respiratory curve for one of the healthy participants who was asked to take a deep breath and also do breath holding.
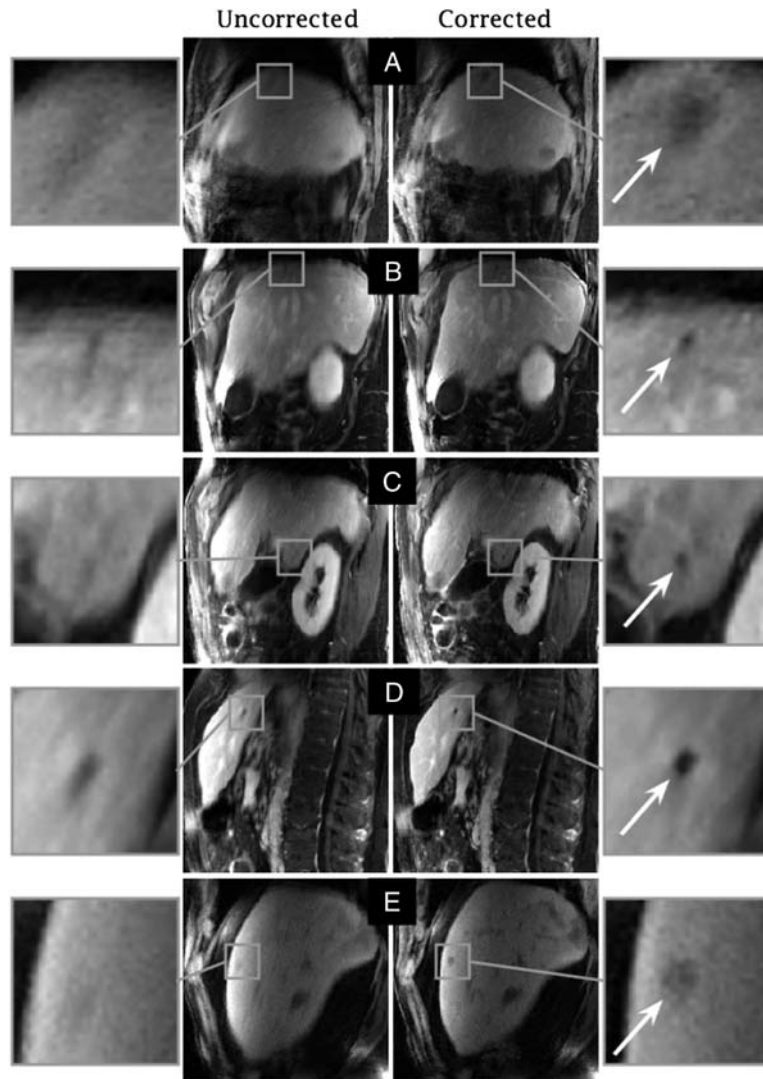
FIGURE 12. Five representative slices from 3 liver tumor patients (A, slice 28 from patient 2; B–D, slices 27, 37, and 58 from patient 3; E, slice 25 from patient 12). Respiratory motion can blur small lesions, but the conspicuity of the lesions was substantially improved by CAPTURE as marked by the white arrows in the magnified inlet images. The major axis lengths of the lesions in the motion-corrected images are roughly (A) 15 mm, (B) 6 mm, (C) 7 mm, (D) 7 mm, and (E) 9 mm.
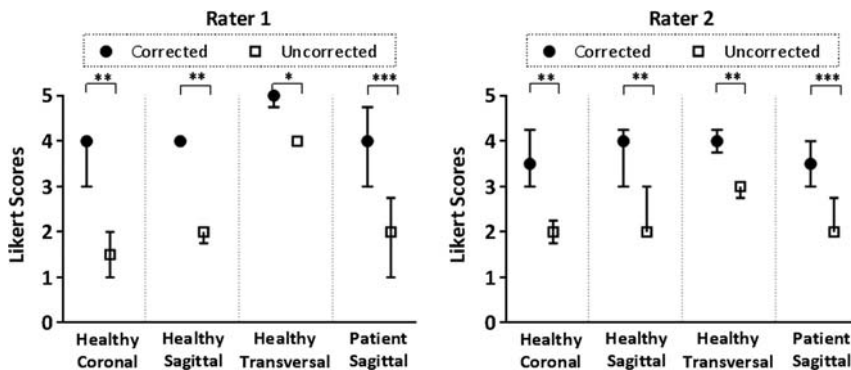

FIGURE 13. Medians and interquartile ranges of the Likert scores given by the 2 raters. According to the Wilcoxon signed-rank test, CAPTURE motion correction results in significantly improved image quality. *$P \leq 0.05$, **$P \leq 0.01$, ***$P \leq 0.001$.

et al[31] can be used for a further reduction of nonphysiological signal contamination at the expense of performing an additional calibration.

CAPTURE is a retrospective motion correction scheme that bins *k*-space data into multiple respiratory phases. Therefore, like all other methods in this category, the sharpness of the images at any given respiratory phase depends on the motion range covered by the corresponding bin. The motion ranges can be reduced by increasing the number of respiratory bins, but this approach may be applied at the expense of a higher amount of streaking artifacts attributable to greater levels of undersampling.

Finally, the deformable motion fields derived from the 4-D motion-resolved images of CAPTURE might be used for improving radiotherapy planning, which helps protect patients from receiving excessive radiation dose.[32] The motion fields can also be used for applying motion correction to the PET data acquired simultaneously as part of a PET/MRI study.

In conclusion, CAPTURE provides a robust and fully automated solution for obtaining 4-D motion-resolved images in a free-breathing setting. With its unique tuning feature, CAPTURE can adapt to large intersubject and interscan variations. CAPTURE also enables better lesion delineation because of improved image sharpness, thereby increasing the visibility of small lesions.

REFERENCES

1. Paling MR, Brookeman JR. Respiration artifacts in MR imaging: reduction by breath holding. *J Comput Assist Tomogr*. 1986;10:1080–1082.
2. Ehman RL, McNamara MT, Pallack M, et al. Magnetic resonance imaging with respiratory gating: techniques and advantages. *AJR Am J Roentgenol*. 1984;143:1175–1182.
3. Lau D, Chen Z, Teo JT, et al. Intensity-modulated microbend fiber optic sensor for respiratory monitoring and gating during MRI. *IEEE Trans Biomed Eng*. 2013;60:2655–2662.
4. Santelli C, Nezafat R, Goddu B, et al. Respiratory bellows revisited for motion compensation: preliminary experience for cardiovascular MR. *Magn Reson Med*. 2011;65:1097–1102.
5. Chen B, Webber N, Odille F, et al. Design and validation of a novel MR-compatible sensor for respiratory motion modeling and correction. *IEEE Trans Biomed Eng*. 2017;64:123–133.
6. Ehman RL, Felmlee JP. Adaptive technique for high-definition MR imaging of moving structures. *Radiology*. 1989;173:255–263.
7. Song H, Ruan D, Liu W, et al. Respiratory motion prediction and prospective correction for free-breathing arterial spin-labeled perfusion MRI of the kidneys. *Med Phys*. 2017;44:962–973.
8. Tibiletti M, Paul J, Bianchi A, et al. Multistage three-dimensional UTE lung imaging by image-based self-gating. *Magn Reson Med*. 2016;75:1324–1332.
9. Jiang W, Ong F, Johnson KM, et al. Motion robust high resolution 3D free-breathing pulmonary MRI using dynamic 3D image self-navigator. *Magn Reson Med*. 2017.
10. Lin W, Guo J, Rosen MA, et al. Respiratory motion-compensated radial dynamic contrast-enhanced (DCE)-MRI of chest and abdominal lesions. *Magn Reson Med*. 2008;60:1135–1146.
11. Grimm R, Fürst S, Souvatzoglou M, et al. Self-gated MRI motion modeling for respiratory motion compensation in integrated PET/MRI. *Med Image Anal*. 2015;19:110–120.
12. Piccini D, Feng L, Bonanno G, et al. Four-dimensional respiratory motion-resolved whole heart coronary MR angiography. *Magn Reson Med*. 2017;77:1473–1484.
13. Higano NS, Hahn AD, Tkach JA, et al. Retrospective respiratory self-gating and removal of bulk motion in pulmonary UTE MRI of neonates and adults. *Magn Reson Med*. 2017;77:1284–1295.
14. Buerger C, Clough RE, King AP, et al. Nonrigid motion modeling of the liver from 3-D undersampled self-gated golden-radial phase encoded MRI. *IEEE Trans Med Imaging*. 2012;31:805–815.
15. Feng L, Axel L, Chandarana H, et al. XD-GRASP: golden-angle radial MRI with reconstruction of extra motion-state dimensions using compressed sensing. *Magn Reson Med*. 2016;75:775–788.
16. Chandarana H, Feng L, Ream J, et al. Respiratory motion-resolved compressed sensing reconstruction of free-breathing radial acquisition for dynamic liver magnetic resonance imaging. *Invest Radiol*. 2015;50:749–756.
17. Campbell-Washburn AE, Xue H, Lederman RJ, et al. Real-time distortion correction of spiral and echo planar images using the gradient system impulse response function. *Magn Reson Med*. 2016;75:2278–2285.
18. Paul J, Divkovic E, Wundrak S, et al. High-resolution respiratory self-gated golden angle cardiac MRI: comparison of self-gating methods in combination with k-t SPARSE SENSE. *Magn Reson Med*. 2015;73:292–298.
19. Chandarana H, Block TK, Rosenkrantz AB, et al. Free-breathing radial 3D fat-suppressed T1-weighted gradient echo sequence: a viable alternative for contrast-enhanced liver imaging in patients unable to suspend respiration. *Invest Radiol*. 2011;46:648–653.
20. Kohler T. A projection access scheme for iterative reconstruction based on the golden section. Rome, Italy: *IEEE Symposium Conference Record Nuclear Science 2004*. 2004:3961–3965.
21. Kazantsev IG, Matej S, Lewitt RM. Optimal ordering of projections using permutation matrices and angles between projection subspaces. *Electron Notes Discrete Math*. 2005;20:205–216.
22. Feng L, Grimm R, Block KT, et al. Golden-angle radial sparse parallel MRI: combination of compressed sensing, parallel imaging, and golden-angle radial sampling for fast and flexible dynamic volumetric MRI. *Magn Reson Med*. 2014;72:707–717.
23. Rasche V, Holz D, Proksa R. MR fluoroscopy using projection reconstruction multi-gradient-echo (prMGE) MRI. *Magn Reson Med*. 1999;42:324–334.
24. Eldeniz C, Chen Y, An H. Cosine-modulated acquisition cleans spectra for better respiratory cine. In: *Proceedings of the 24th Annual Meeting of ISMRM*. Singapore: 2016. Abstract #519.
25. Davies SC, Hill AL, Holmes RB, et al. Ultrasound quantitation of respiratory organ motion in the upper abdomen. *Br J Radiol*. 1994;67:1096–1102.
26. Peters DC, Derbyshire JA, McVeigh ER. Centering the projection reconstruction trajectory: Reducing gradient delay errors. *Magn Reson Med*. 2003;50:1–6.
27. Griswold MA, Jakob PM, Heidemann RM, et al. Generalized autocalibrating partially parallel acquisitions (GRAPPA). *Magn Reson Med*. 2002;47:1202–1210.
28. Knoll F, Bredies K, Pock T, et al. Second order total generalized variation (TGV) for MRI. *Magn Reson Med*. 2011;65:480–491.
29. Lustig M, Donoho D, Pauly JM. Sparse MRI: The application of compressed sensing for rapid MR imaging. *Magn Reson Med*. 2007;58:1182–1195.
30. Grimm R, Bauer S, Kiefer B, et al. Optimal channel selection for respiratory self-gating signals. In: *Proceedings of the 21st Annual Meeting of ISMRM*. Salt Lake City, UT: 2013:3749.
31. Moussavi A, Untenberger M, Uecker M, et al. Correction of gradient-induced phase errors in radial MRI. *Magn Reson Med*. 2014;71:308–312.
32. Li G, Citrin D, Camphausen K, et al. Advances in 4D Medical Imaging and 4D Radiation Therapy. *Technol Cancer Res Treat*. 2008;7:67–81.